Analog Multiband: Efficient Bandwidth Scaling for mm-Wave Communication

Hossein Roufarshbaf, *Member, IEEE*, Upamanyu Madhow, *Fellow, IEEE*, Mark Rodwell, *Fellow, IEEE*, and Sridhar Rajagopal, *Senior Member, IEEE*

***Abstract*—We investigate analog multiband as a means of scaling communication bandwidths over dispersive channels: the available band is channelized into contiguous subbands in the analog domain and digitized in parallel at the receiver. The subband width is chosen such that existing analog-to-digital converter (ADC) technology provides dynamic range sufficient to capture the effects of channel dispersion and interband interference. This avoids the difficulty of scaling high-precision ADCs to large bandwidths, while allowing the use of sophisticated digital signal processing (DSP) techniques for all transceiver operations except for channelization. In this paper, we address two fundamental bottlenecks associated with this concept. The first is channelization. A direct approach using a bank of mixers with independent frequency synthesizers is power-inefficient and subject to oscillator coupling, hence we explore an alternative approach based on polyphase sampling and sampled analog fast Fourier transform (FFT), along with appropriately designed baseband filters. The second is interference due to imperfect channelization (in the interest of bandwidth efficiency, we do not use guard bands) and imperfections in analog processing. We characterize the unique structure of this interference when OFDM is used over each subband, and show that linear adaptive interference suppression on the edge subcarriers suffices to provide robust performance. MultiGigabit/s millimeter (mm) wave communication is a key application driver for this work, hence we illustrate our ideas with performance evaluation using indoor channel models developed for the IEEE 802.11ad 60 GHz standard.**

***Index Terms*—Analog multiband, filter banks, millimeter wave communication, 60GHz wireless communications.**

I. Introduction

With recent advances in radio frequency integrated circuits (RFICs) in the millimeter wave band, 10s of GHz of spectrum have become commercially viable. In particular, the 60 GHz unlicensed band has in particular received significant attention, with significant impetus provided by the development of the IEEE 802.11ad standard for multiGigabits per second wireless local area networks (WLANs) [1]. In addition, there is significant interest in mm wave 5G cellular systems [2]–[4], including potential extension of 60 GHz base station to mobile links in outdoor picocellular networks [5]. A key challenge in scaling up communication bandwidths in such systems is the ADC. The modern "mostly digital" paradigm for transceiver design, where most sophisticated functions are performed using digital signal processing (DSP), relies on the availability of ADCs with sufficient dynamic range. This is difficult to attain at high sampling rates, especially when constrained by cost and power as in the above mentioned emerging commercial applications, which center around mobile devices.

In this paper, we investigate analog channelization into subbands as a means of scaling up communication bandwidths. Each subband has small enough bandwidth so that existing ADC technology at moderate sampling rates (i.e. 500 MS/s to 1.0 GS/s) can be used, providing a dynamic range sufficient to capture the effects of both interband and intersymbol interference. Thus, DSP-centric techniques can be used for all transceiver functions other than channelization, which allows us to continue taking advantage of Moore's law as communication bandwidths increase. Furthermore, as ADC technology evolves, subband widths can be increased, so that the overall system bandwidth can be increased for a given number of subbands. We term this approach *analog multiband.* Any form of modulation can be used over each subband, but in this paper, we focus on OFDM, which has become the de facto standard for DSP-centric design for dispersive channels (in the typical settings we consider, the subband widths are larger than the channel coherence bandwidth, hence the channel over each subband is dispersive).

Contributions: Our main contributions are as follows: 1) While analog channelization can be achieved, in principle, by a bank of mixers, this is costly and power-inefficient, and subject to problems such as oscillator coupling. We therefore consider two alternative techniques based on polyphase sampling: a direct approach based on the harmonic rejection mixer (HRM), as well as a more efficient indirect approach using polyphase filters and fast Fourier transform (FFT) implemented in the sampled analog domain (discrete-time, continuous-range processing). While polyphase sampling and parallel processing in this fashion bears some similarity to the time-interleaved (TI) ADC, which has become the most common architecture for pushing the limits of ADC speeds (see recent references in [6]), our approach may be viewed as an alternative frequency domain parallelization which relaxes the specifications for the component ADCs, at the cost of more analog processing. That is, unlike the sub-ADCs in a time-interleaved architecture, each

Manuscript received May 29, 2015; revised October 28, 2015; accepted January 29, 2016. Date of publication February 26, 2016; date of current version April 14, 2016. This work was supported in part by Samsung Research America—Dallas, and in part by the National Science Foundation under Grant CNS-1518812. The guest editor coordinating the review of this manuscript and approving it for publication was Prof. Akbar Sayeed.

H. Roufarshbaf, U. Madhow, and M. Rodwell are with the University of California, Santa Barbara, Santa Barbara, CA 93106-9560 USA (e-mail: hroufarshbaf@ece.ucsb.edu; madhow@ece.ucsb.edu; rodwell@ece.ucsb.edu).

S. Rajagopal is with Samsung Research America—Dallas, Dallas, TX 75082, USA (e-mail: sridhar.r@samsung.com).

Color versions of one or more of the figures in this paper are available online at http://ieeexplore.ieee.org.

Digital Object Identifier 10.1109/JSTSP.2016.2535184

of which sees the entire dynamic range, the component ADCs in our approach see a smaller dynamic range governed mainly by signal fluctuations within a subband.

2) We consider a spectrally efficient guardband-free channelization scheme, hence inter-band interference is a significant impairment which can produce error floors if left uncompensated. We characterize the specific structure of interference when OFDM is employed over each subband, including the effect of timing mismatch in our sampling-based channelizer. Each subcarrier in a subband sees interference only from corresponding subcarriers in other subbands. Furthermore, for appropriately designed baseband filters, inter-band interference is restricted to the edge subcarriers in each subband, and can be effectively suppressed by linear adaptive techniques operating in parallel over the affected subcarriers.

3) While the proposed approach is quite general, for our simulation results, we focus on indoor 60 GHz channel models developed under the IEEE 802.11ad standardization process. We observe that, even after beamforming along the strongest path, the residual channel dispersion within a subband of 250-500 MHz width is several symbols long. Thus, OFDM within a subband as we have assumed here is a robust design choice, although it is also of great interest to explore single carrier techniques in view of their smaller peak-to-average ratio.

Related work: Analog multicarrier techniques, with subcarrier widths small compared to the coherence bandwidth, were considered decades ago, but became obsolete when all-digital implementations of OFDM became possible. However, OFDM relies on ADCs with high dynamic range in view of its large peak-to-average ratio, which presents difficulties as the communication bandwidth scales up. This has motivated investigation of analog multiband for high-speed applications such wired backplane [7], [8] and optical channels [9], [10] in recent years. An analog multiband communication scheme over 60 GHz channel is also presented in [11]. However, all of these schemes separate the subbands enough that inter-band interference is negligible, unlike our spectrally efficient guardband-free approach. Analog multiband without guard band insertion has also been studied in [12] (where the approach was termed analog multitone), but single carrier modulation over each subband was considered. Linear interference suppression is found to be effective there as well, but the interference structure is different from our OFDM setting, and time domain techniques are used. Moreover, the challenge of efficient channelization is not considered in [12]. The advantages of sampled analog FFT for reducing the required ADC dynamic range for ultra-wideband OFDM systems is explored in [13], which shows that performance superior to that of FFT with moderate precision ADC can be obtained even with mismatch and jitter in the sampled analog FFT components. While the sampled analog FFT in [13] is intended to separate out subcarriers that see frequency non-selective channels, we use the sampled analog FFT to separate out subbands which each see channel dispersion and inter-band interference, addressed by using OFDM within subbands and per-subcarrier interference suppression.

A natural alternative to the proposed architecture is an all-digital receiver [14]. Many of the highest speed ADCs today are based on a time-interleaved architecture [6]. Given that both our architecture and the TI-ADC require high-speed analog sample-and-hold circuitry with adequate dynamic range and good noise characteristics, we can leverage the significant advances in TI-ADC technology over the last decade. The main advantage of our proposed architecture is in the reduction of dynamic range prior to digitization, but this comes at the cost of additional analog processing. While detailed circuit-level tradeoffs beyond our present scope must be investigated to determine the right choice in any given context, we believe that the proposed approach is a serious alternative worth exploring as we push the limits of speed in communication systems.

We note that the problem of digitization for communication differs fundamentally from that of digitizing natural signals. Many high-dimensional natural signals are sparse in some basis or manifold, which makes compressive data acquisition techniques such as Xsampling [15] attractive. However, in spectrally efficient communication as considered here, we try to use all of the degrees of freedom available in the signal space, hence compressive techniques do not apply for information recovery. However, since the communication channel (given by nature) can be sparse, compressive techniques can be quite effective for channel estimation [16], [17], possibly including the setting considered here. Detailed discussion of channel estimation is outside our present scope, but integrating it into the overall system design is an important topic for future work.

We should note the significant recent interest in exploring *digital* multiband modulation techniques for 5G wireless, under terms such as filterbank multicarrier (FBMC) [14], universal filterbank multicarrier (UFMC) [18], and generalized frequency division multiplexing (GFDM) [19]. The goal of these techniques is typically to reduce peak-to-average ratios, to enable flexible channelization across multiple users, and to reduce or eliminate cyclic prefix overhead. However, the primary focus of our *analog* design scheme is power efficiency and efficient channelization without guardband insertion.

The present paper integrates results from our prior conference papers [20] (focusing on interference modeling and suppression) and [21] (focusing on channelization). It goes beyond [20], [21] by studying the effect of timing mismatch and different prototype filters on sampling-based channelization. This includes characterizing the structure of the resulting interference, and the performance with and without interference suppression.

II. Analog Multiband Structure

Fig. 1 shows the baseband equivalent model of the proposed analog multiband structure. The total bandwidth is broken into M parallel subbands, so that the input data is demultiplexed into M streams, each sent over a different subband. The modulation over each subband can be freely chosen, but in this paper, we focus on OFDM with cyclic prefix (CP). As discussed in Section VI-B, the delay spread of the indoor mm-wave channel even after beamforming still spans several symbols at the subband level. Thus, while single carrier techniques are very much worth exploring given their smaller dynamic range, we focus here on OFDM/CP as a robust, technologically mature choice for handling subband-level inter-symbol interference (ISI).

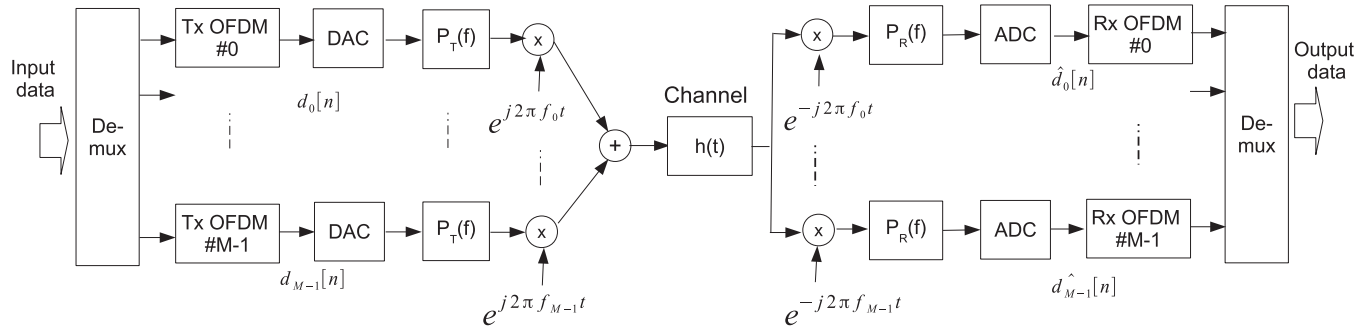

Fig. 1. Analog multiband block diagram for bandwidth scaling at mm-wave through spectrum channelization. Data symbols are demultiplexed into M subbands. Each subband is an OFDM communication block diagram and a mixer banks is used to line up the subband spectrums in frequency domain.

The modulated signal of each subband (OFDM samples in our case) are passed through the pulse shape filter (transmit filter) and are stacked up in frequency domain, spaced at Δf. We assume that there is no guardband between the subbands, hence $\Delta f = 1/T$, the sampling rate within each subband. At the receiver, the subbands are separated out in the analog domain, and then digitized in parallel by ADCs, each running at rate $1/T$. Fig. 1 shows this channelization at the conceptual level, using a bank of mixers at both transmitter and receiver, but more practical approaches to channelization are discussed in the next section. The digitized signals are then processed for OFDM demodulation and inter-band interference suppression.

We now establish mathematical notation for the conceptual block diagram in Fig. 1. Since our discussion of analog channelization in the next section is independent of the subband-level modulation format, we do not make any assumptions about the latter yet. We denote the rate $1/T$ samples to be transmitted on subband k by $d_k[n]$, where $k = 0, \cdots, M-1$. (For OFDM on each subband, these are the serialized outputs of the OFDM IDFT block, along with the CP.) For each subband, these samples are passed through a pulse shaping filter $p_T(t)$ and then shifted in frequency appropriately before summing. The transmitted signal is an aggregate of these pulse-shaped/frequency-shifted subband signals as follows:

$$\begin{aligned} x(t) &= \sum_n \sum_{k=0}^{M-1} d_k[n] p_T(t - nT) e^{j2\pi(t-nT)f_k} \\ &= \sum_n \sum_{k=0}^{M-1} d_k[n] p_{T,k}(t - nT), \end{aligned} \tag{1}$$

where $p_{T,k}(t - nT)$ is the frequency shifted transmit pulse shaping filter defined as

$$p_{T,k}(t) = p_T(t) e^{j2\pi t f_k}. \tag{2}$$

The preceding transmitted signal formulation is similar to the standard FBMC formulation [22]. However, the key difference in our model is the manner in which this conceptual system model is actually realized using analog channelization, and the explicit characterization and suppression of inter-band interference when OFDM is used over each subband. Given an ideal channel and noise, the received samples are equal to the transmitted samples when

$$\int_{-\infty}^{\infty} p_{T,k}(t - mT) p^*_{R,l}(t - nT) dt = \delta_{kl}\delta_{mn}, \tag{3}$$

where δ is the Kronecker delta function and

$$p_{R,k}(t) = p_R(t) e^{j2\pi t f_k} \tag{4}$$

is the frequency shifted receive filter on subband k. When there is nontrivial channel dispersion, the effective channel model obtained by cascading the transmit filter, channel impulse response, and the receive filter must be calculated for analysis of the inter-symbol and inter-band interference. As discussed in Section IV, while the ISI is handled as usual within each subband by CP insertion in OFDM signal, the sidelobe behavior of the transmit and receive filters dictates the level of the inter-band interference.

While the block diagram in Fig. 1 conveys the concept of parallelization in analog multiband, a direct approach to analog channelization using banks of independent mixers at the transmitter and receiver can be unattractive, due to oscillator coupling, pulling, spur coupling and high power consumption [23]. In the following section, we adapt recently developed ideas in polyphase sampling and mixing [24] for efficient channelization in our setting. These are then evaluated, taking into account imperfections due to timing mismatch, in later sections, in the context of indoor 60 GHz communication.

III. Sampling-Based Channelization

Sampling-based channelization synthesizes multiple mixer outputs from linear transformations of polyphase samples obtained based on a single master clock. Two such techniques are the harmonic rejection mixer (HRM) bank [23], [25] and the sampled analog fast Fourier transform (FFT) [13]. Either of these can be applied in our setting, but as we discuss, the second approach is more attractive.

An interesting alternative worth exploring in future work is the use of passive channelization techniques: recent work in [26], [27] reports use of passive channelization techniques for bandwidth less than 100 MHz, hence their application for multi-GHz bandwidths remains an open question.

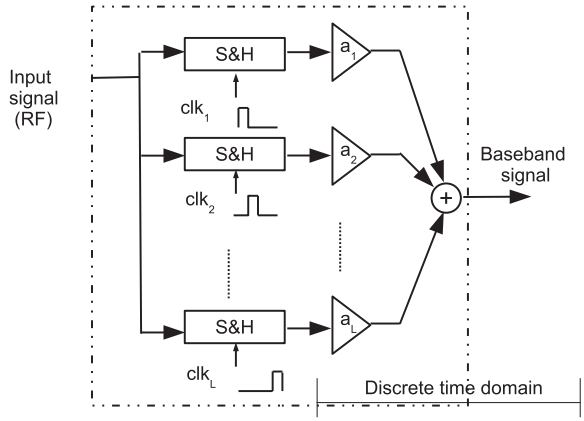

Fig. 2. The structure of a HRM polyphase mixer. The signal is sampled in the upper rate of Lf_{LO}, where each sample is phase-shifted in time by $1/Lf_{LO}$. The sample and hold operation (S&H) keeps each sampled signal until the signal in the next path is sampled. The sampled signal in each path is multiplied by coefficients a_l as given in (5).

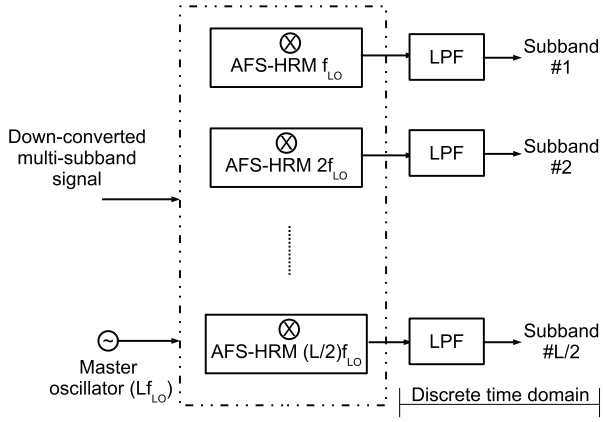

Fig. 3. The proposed channelizer scheme with L/2 harmonic rejection mixers generated from a master clock with frequency Lf_{LO}.

A. Direct Channelization Using Harmonic Rejection Mixer Bank

In a frequency synthesis harmonic rejection mixer bank, frequencies of mf_{LO}, $m = 1, \ldots, L/2$ are synthesized from a master clock of frequency Lf_{LO}. The HRM overcomes mixer nonlinearities by removing the major odd harmonics, as well as all even harmonics of the output signal. Fig. 2 shows the structure of a HRM which can be tuned on the frequencies mf_{LO}. In order to mix a signal against a frequency mf_{LO}, we sample it at rate Lf_{LO}. Each signal sample (sample l) is held and multiplied by a gain coefficient a_l^m given by

$$a_l^m = \sin\left(\frac{2\pi lm}{L}\right) \quad \begin{matrix} l = 1, \cdots, L \quad \text{and} \\ m = 1, \cdots, L/2 \end{matrix}. \tag{5}$$

By appropriately selecting the coefficients, all harmonic frequencies except for $nL \pm m$ (n is any integer number) are rejected, so that the weighted signal samples correspond to the input signal mixed against mf_{LO}, as long as the input signal bandwidth is small enough compared to Lf_{LO}.

To generate a bank of mixers, as is required for subband channelization, one can synthesize all frequencies from f_{LO} to $(L/2)f_{LO}$ from the master clock Lf_{LO} (Fig. 3). In comparison to the traditional bank of L independent mixers, the advantage in using the AFS-HRM structure is that only a single master oscillator is required. Thus, oscillator coupling issues do not arise, and the system is significantly more power-efficient. It should be noted that the mixer conversion gain for each synthesized frequency is slightly different. While these must be compensated for in general, for our communications applications, variations in gains across subbands can be compensated for in DSP, and are therefore irrelevant.

B. Indirect Channelization Using Sampled Analog FFT

An alternative to the HRM bank, also using polyphase sampling and linear processing, is the analog DFT (together with polyphase filters). This is especially attractive when the number of subbands is a power of 2, since the IDFT and DFT can be implemented with $O(M \log_2 M)$ complexity using the butterfly structure [13]. As a first step to deriving this structure, let us start with a discrete time equivalent model, shown in Fig. 4, for this filtered multitone approach, which was first introduced for very high speed digital subscriber line (VDSL) in [28]. Fig. 4 looks like a discretized version of the conceptual block diagram for analog multiband in Fig. 1, with a key difference being the upsampling step. The bandwidth of the transmitted signal in each subband is approximately $1/T$. The signal is upsampled by the factor K, where $K \geq M$ (M is the number of subbands), and unwanted aliased copies are rejected by the lowpass pulse shaping filter. We then translate the center frequency of subband m to $f_m = mK/TM$ ($m = 0, \cdots, M-1$), and the parallel-to-serial converter adds up these signals so as to cover the entire bandwidth. The distance between the adjacent subbands is $\frac{K}{TM}$ and the ratio K/M determines the guard band between the subbands, which becomes zero for the special case $K = M$, termed the "critical condition" in [28]. Since we are interested in maximizing spectral efficiency, we operate in the latter regime, setting $K = M$, and handling spectral leakage across subbands using interference suppression.

We now show how the architecture depicted in Fig. 4 can be implemented efficiently using IDFT plus polyphase filtering. Consider the discrete-time model of the transmitted signal in (1) at time kT/M:

$$x\left(k\frac{T}{M}\right) = \sum_{m=0}^{M-1} \sum_{n=-\infty}^{\infty} d_m[n] p_T\left[(k - nM)\frac{T}{M}\right] e^{j2\pi mk/M}. \tag{6}$$

Now, by changing the order of summation and applying the change of variable $kT/M = lT + i(T/M)$ where $i = 0, 1, \cdots, M-1$, the output signal is given by

$$x\left(lT + i\frac{T}{M}\right) = \sum_{n=-\infty}^{\infty} \left(\sum_{m=0}^{M-1} d_m(nT) e^{j2\pi mi/M}\right) p_T\left[(l-n)T + i\frac{T}{M}\right]. \tag{7}$$

The inner summation in (6) is the IDFT of the subband symbols, and the term $p_T[(l-n)T + i\frac{T}{M}]$ is the ith polyphase

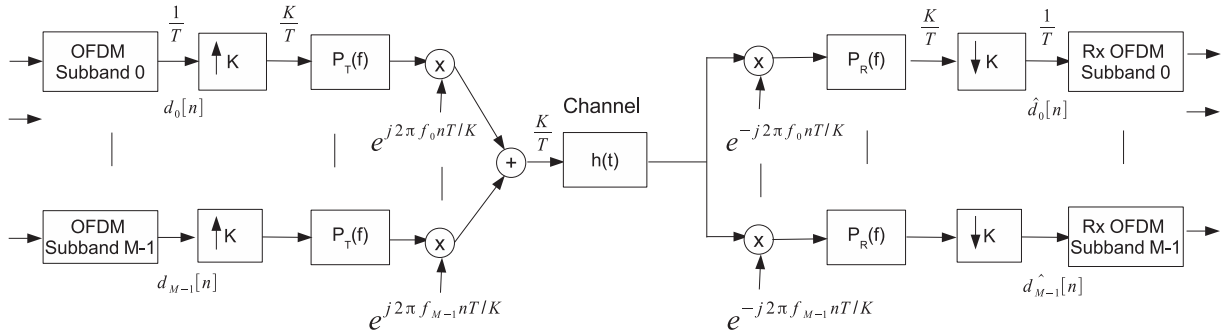

Fig. 4. The FMT channelizer scheme with OFDM subbands.

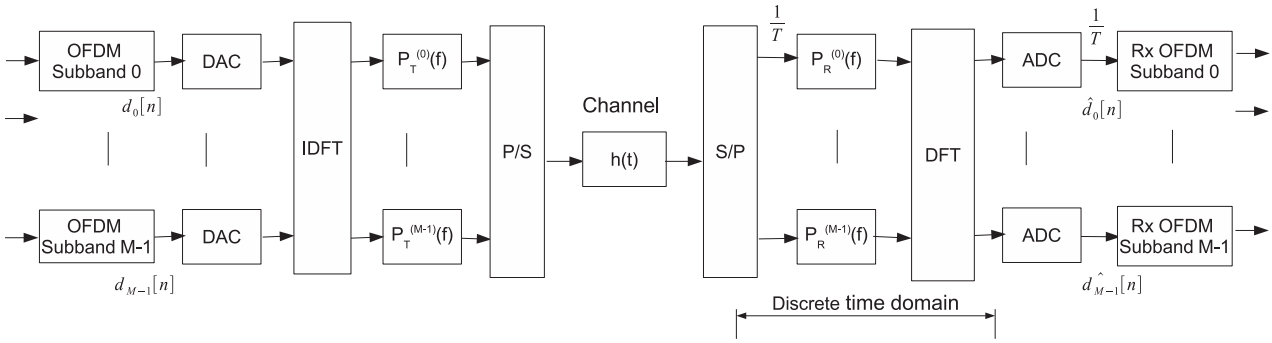

Fig. 5. The proposed FMT channelizer in the critical condition ($K = M$ in comparison to Fig. 4) with sampled analog IDFT/FFT.

component of the transmit filter. This suggests that the transmitter block diagram can be modified to perform the IDFT first, and then apply the pulse shaping filter on each output of the IDFT block, followed by a serial-to-parallel conversion. Of course, interleaving the signals from the different subbands (instead of summing upsampled versions as in Fig. 4) requires that the filters for different subbands must be slightly different: the impulse responses for these polyphase filters are simply samples of a common continuous time baseband filter, offset by different phases for different subbands. The modified transmitter block diagram is shown in Fig. 5.

We can follow the same procedure at the receiving side to apply the DFT block for subband separation. Following the FMT block diagram (Fig. 4), the signal for subband i is given by

$$\hat{d}_i(nT) = \sum_{k=-\infty}^{\infty} y\left(k\frac{T}{M}\right) e^{-j2\pi f_i kT/M} p_R\left(k\frac{T}{M} - nT\right). \tag{8}$$

Letting $kT/M = lT + mT/M$ and $m = 0, \cdots, M-1$ which models polyphase sampling of the received signal, the sum in (8) can be break down into two summations as follows

$$\hat{d}_i(nT) = \sum_{m=0}^{M-1} \sum_{l=-\infty}^{\infty} y\left(lT + m\frac{T}{M}\right) p_R\left[(n-l)T - m\frac{T}{M}\right] e^{-j2\pi mi/M}. \tag{9}$$

The preceding equation suggests modifying the receiver block diagram based on polyphase sampling as shown in Fig. 5, with polyphase samples filtered with the pulse shaping filters corresponding to different subbands, and then performing subband separation via the DFT block.

C. Peak-to-Average Power Ratio

The sum of independent signals sent over subbands, regardless of the technique used for channelization, inevitably increases peak-to-average power ratio (PAR), which is defined [29] for a signal $x(t)$ as

$$\epsilon_0 = \frac{\max |x(t)|^2}{E\{|x(t)|^2\}}, \tag{10}$$

where $E\{\}$ denotes expectation, and is replaced by an empirical average when computing PAR for a given signal realization.

For the system in Fig. 5, the maximum PAR for the OFDM samples of each subband with N subcarriers is $10\log(N)dB$ [29]. For M subbands, the maximum PAR of the transmitted signal increases by $10\log(M)dB$. As such, this is no better than single carrier OFDM with MN subcarriers. There are two complementary approaches to alleviate this. The first is not to use OFDM over each subband (a choice we have made simply because of the maturity of the technology), but to consider single carrier techniques with low PAR. The second is to reduce the dynamic range requirement for the receiver's ADC by demultiplexing the channels prior to the ADC. The sampled analog FFT performs this function, so that the low-rate ADCs for each subband only need sufficient dynamic range to accommodate that subchannel (plus the relatively small PAR increase due to interference from adjacent subbands). Thus, the subband ADCs in such an approach need dynamic range

that is $\log_2 M$ smaller than the sub-ADCs in a time-interleaved architecture for direct digitization, which is expected to lead to lower power consumption and better linearity properties. While these observations hold for ideal analog channelization, we provide numerical results in Section VI-B that show the significant decrease in dynamic range requirements after the analog DFT, taking into account imperfections due to mm-wave indoor channel.

D. Discussion

Variations of filterbank multicarrier modulations, widely used in high speed xDSL [28], have been recently revisited for wireless communication [22] as well as optical communication systems (wavelength division multiplexing) [30], in order to alleviate synchronization requirements for OFDMA, and to remove the requirement for CP insertion when we put the subbands together (in contrast with what would happen if OFDM were used over the entire band). However, in all of these applications, the ADC is applied at the first step, prior to serial-to-parallel conversion, and subband separation is performed purely digitally.

Given the difficulty in scaling ADCs to large bandwidth, we observe that sampling rate reduction through analog parallelization is a key factor in efficient design. Let us examine several potential receiver architectures for analog multiband modulation at mm-wave carrier frequencies, with channel bandwidth of the order of 5 GHz. Suppose that the sub-bands are of width 250-500 MHz. The receiver would first downconvert the received RF signal to baseband, either through direct conversion or by superheterodyne. A baseband processor then recovers and digitizes the separate sub-channels Fig. 6. While detailed hardware design is beyond our current scope, we now provide a high-level discussion of a number of implementation options, indicating why we have chosen to study sampler-based analog separation of the bands.

One method to recover each individual subband is to separately downconvert each subband frequency to DC, as in Fig. 6(a). The resulting demodulated subband is then digitized. There are several difficulties in realizing this structure in monolithic form. First, it is difficult to realize analog LC filters of the necessary quality, given the target 0.25-5 GHz center frequencies and ~250-500 MHz bandwidths. On-chip inductors and capacitors are physically too large, and their Q (particularly for inductors) is too low; it is hard to obtain the necessary steep filter skirts, nor the necessary in-band gain flatness. The target passband frequencies are too high for op-amp active filters, as these demand op-amp unity-gain frequencies well more than 10 times the filter upper cutoff frequency. Low-pass $g_m - C$ filters [31] have been demonstrated to 10 GHz, but the feasible operating frequency of high-selectivity band-pass $g_m - C$ filters is smaller because of the need for high-Q filter poles and the resulting filter sensitivity to excess transistor phase shift. An additional difficulty lies with the mixer local oscillators. With equally spaced subbands, these lie in a $f_0, 2f_0, 3f_0, \ldots$ sequence. As these cannot be readily generated from a series of counters operating from a single master clock, a series of synthesizers, as discussed in Section III-A, are instead required. Between filters, LO synthesizers, and mixers, the resulting hardware is complex.

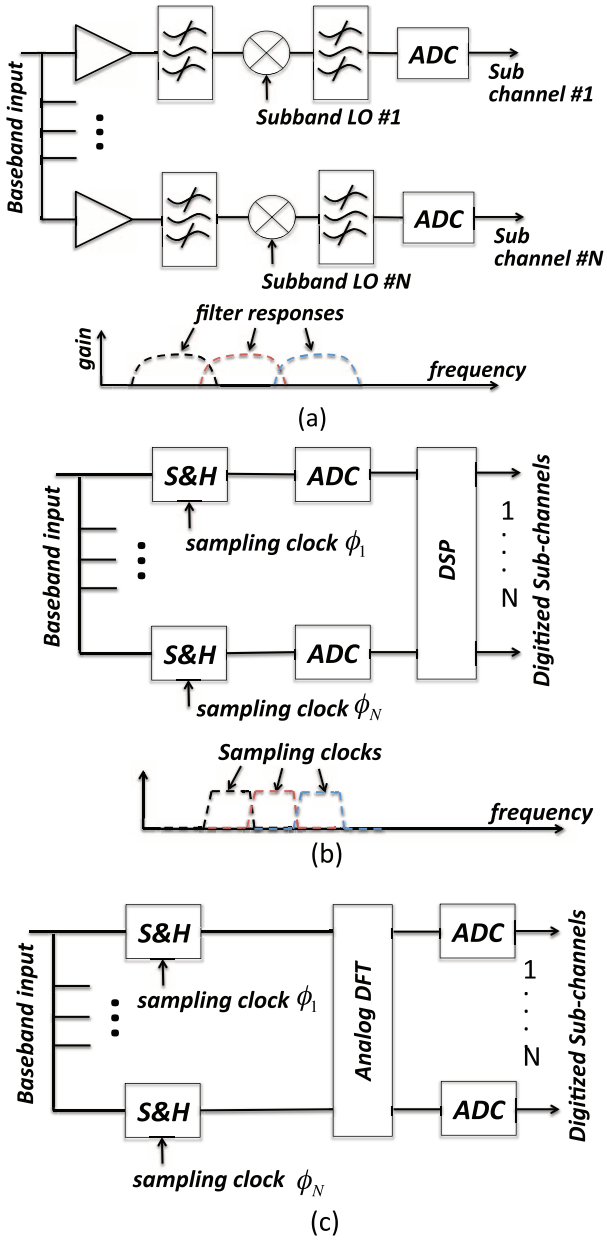

Fig. 6. Candidate receiver architectures for analog multiband. After the receiver front-end downconverts the received signal, the individual subbands are recovered (a) by filtering in frequency and separately down-converting and digitizing each subband, (b) by acquiring the baseband signal with a time-interleaved ADC and subsequently separating and recovering the subbands by digital signal processing, or (c) by separating the frequency bands by an analog discrete Fourier transform and subsequently digitizing each subband.

A second, common implementation is to digitize the signal and subsequently separate and demodulate the subbands by digital signal processing, as in Fig. 6(b). As shown in the figure, if the channel bandwidth is large, the digitizer can be time-interleaved [32]. Channel-channel mismatches in the ADC array can be addressed directly in DSP [33]. While this architecture is favorable at low and moderate channel bandwidths, for high aggregate channel bandwidths the power consumption

of high-speed digital signal processing may be large. Note that the N-phase sampling clocks in the time-interleaved ADC are readily and simply generated with a master oscillator, binary counter, and N-output binary decoder.

A third implementation shown in Fig. 6(c), which is the one suggested in this paper, is to separate the signals by frequency-domain filtering using analog discrete-time circuits. In this topology, as with a time-interleaved ADC, the signal is first sampled with an array of analog sample-holds gated by an N-phase set of non-overlapping clocks. In this architecture, dynamic range requirements of the sample-holds are similar to those of the time-interleaved ADC. The overall demodulated signal is separated into frequency bands using a bank of analog discrete-time filters, with the filters formed by summation (9) of the sample-hold outputs. The sample-hold gates and summation network form a set of band-pass filters; as the sample-hold gates can be formed from FET sampling switches and the summation network from a set of weighted FET g_m elements, the resulting filter network is more suited to compact IC implementation than a set of LC filters (Fig. 6-a). The filter outputs are then digitized by low-speed ADCs, with each filter output and ADC carrying the bandwidth of a single subcarrier.

Sample and hold circuitry: The proposed architecture employs a sample-and-hold block for serial to parallel conversion which must have sufficient dynamic range to support linear and low noise signal acquisition. Fortunately, recent advances in multi-Gsamples/sec TI-ADC [34], [35], which also employ sample-and-hold circuitry, imply that it is indeed possible to design high-speed sample-and-hold with reasonable power consumption and good dynamic range. Other recent examples of high-speed/high-resolution sample-and-hold ICs include [36] and [37], operating at rates above 15 GS/s and 32 GS/s, respectively.

Noise considerations: Since we employ mixed signal processing after conversion to baseband, the proposed architecture is not subject to noise folding, in contrast to techniques that employ sub-sampling as a means of direct conversion [38]. Addition of the sample and hold circuitry and sampled analog FFT increases the analog circuit noise, which must be studied in the context of specific circuit-level implementations beyond our present scope. Relevant studies in the literature include noise analysis for HRM mixer bank in [23] and for sampled analog FFT in [13].

IV. Interference Analysis

We now explore the structure of inter-band interference, assuming tight subband packing with no guard bands. The key observation is that, when we employ OFDM modulation over subbands, each subcarrier in a subband sees interference only from the corresponding subcarriers in other subbands. Furthermore, for well-designed baseband filters, as expected, only edge subcarriers see interference. Thus, per-subcarrier linear interference suppression strategies deployed only over the edge subcarriers suffice.

For simplicity of exposition, we work with the conceptual block diagram shown in Fig. 1 (which uses a bank of mixers) in this section. We then discuss in Section V how this approach naturally extends to handle the additional interference resulting from timing mismatches in sampling-based channelization as in Fig. 5.

A. Interference Model

Each subband uses OFDM with N subcarriers, a cyclic prefix of length L, and a sampling rate of $1/T$. There are M subbands. We denote the OFDM symbol l for subband m which includes the cyclic prefix with length of L samples by

$$\mathbf{d}_m^l = [d_m(lN - L + 1), \cdots, d_m(lN), \\ d_m((l-1)N + 1), \cdots, d_m(lN)], \quad (11)$$

where $d_m(n)$ is the nth sample (corresponding to subcarrier n) at the output of the IDFT block of the OFDM transmitter on subband m.

We assume that the baseband filters, while not ideal, are designed well enough that interference from a subband only spills onto the immediately adjacent subbands, even without guard bands. This assumption has been verified to hold for SRRC and Gaussian filters, but does not hold for spectrally inefficient rectangular time limited impulse responses, for example. (See discussion in Section VI-F). Focusing, therefore, on a designated subband m, we only model interference from subbands $m-1$ and $m+1$.

For the system block diagram in Fig. 1, the equivalent channel $\mathbf{h}_{eq}$ for subband m is the cascade of the transmit filter for subband m, the channel impulse response, and the receive filter for subband m. Similarly, the equivalent cross-talk channel from subband $m+1$ to subband m is denoted by $\mathbf{h}_{eq}^+$, and that from subband $m-1$ to subband m is denoted by $\mathbf{h}_{eq}^-$. These are, respectively, the cascade of the transmit filter of subband $m \pm 1$, the channel impulse response, and the receive filter of subband m. We assume that the same set of transmit/receive filters, shifted appropriately in frequency to the center of each subband, are used for all subbands. parallel channels (of course tuned to a different frequency band), hence the preceding equivalent channels are independent of m, and are given by

$$\mathbf{h}_{eq} = p_T * h * p_R \quad (12)$$

$$\mathbf{h}_{eq}^+ = (p_T e^{-j2\pi\Delta f t}) * h * p_R \quad (13)$$

$$\mathbf{h}_{eq}^- = (p_T e^{j2\pi\Delta f t}) * h * p_R, \quad (14)$$

where $*$ denotes the convolution operation, h is the impulse response of the channel and p_T and p_R denote the impulse response of the transmit and receive filters (Fig. 1), respectively. Note that the interference channel $\mathbf{h}_{eq}^-$ is equal to zero for the first subband ($m = 0$) and $\mathbf{h}_{eq}^+$ is equal to zero for the last subband ($m = M-1$), but our interference analysis focuses on a typical subband in the middle of the band which sees interference from adjacent subbands on both sides.

The received signal of subband m after analog to digital conversion is now modeled as

$$\mathbf{y}_m^l = \mathbf{h_{eq}} * \mathbf{d}_m^l + \mathbf{h}_{eq}^+ * \mathbf{d}_{m-1}^l + \mathbf{h}_{eq}^+ * \mathbf{d}_{m+1}^l + \mathbf{w}_m^l, \quad (15)$$

where $\mathbf{w}_m^l$ is the additive white Gaussian noise. We have assumed here that the OFDM transmitted symbols over parallel subbands are synchronized in time and have the same cyclic prefix length. This ensures that when we remove the cyclic prefix of the received signal on subband m, the cyclic prefix samples of the interfering signals of subband $m-1$ and $m+1$ are also removed and the convolution operation on all right-hand terms of (15) is changed to circular convolution:

$$\mathbf{r}_m^l = \mathbf{h_{eq}} \circledast \mathbf{d}_m^l + \mathbf{h}_{eq}^+ \circledast \mathbf{d}_{m-1}^l + \mathbf{h}_{eq}^+ \circledast \mathbf{d}_{m+1}^l + \mathbf{w}_m^l, \quad (16)$$

where $\circledast$ denotes the circular convolution and $\mathbf{r}_m^l$ is the received OFDM symbol after removing the CP samples. After taking the discrete Fourier transform (DFT), we obtain

$$\mathbf{R}_m^l = \mathbf{H}_{eq}.\mathbf{D}_m^l + \mathbf{H}_{eq}^-.\mathbf{D}_{m-1}^l + \mathbf{H}_{eq}^+.\mathbf{D}_{m+1}^l + \mathbf{W}_m^l, \quad (17)$$

where . denotes element by element multiplication of two vectors, $\mathbf{H}_{eq}$ is the DFT of the equivalent transmit channel, $\mathbf{D}_m^l$ is the DFT of $\mathbf{d}_m^l$, $\mathbf{H}_{eq}^-$ and $\mathbf{H}_{eq}^+$ denote the DFT of the equivalent interfering channels. We observe that, by virtue of the cyclic prefix, the interference seen by OFDM symbol l is only due to OFDM symbol l from each of the neighboring subbands. We can therefore restrict attention to one OFDM symbol at a time, and drop the index l from our notation. Rewriting (17) for OFDM subcarrier n, the received signal is given by

$$\begin{aligned} R_m(n) = {} & H_{eq}(n).D_m(n) + H_{eq}(n)^-.D_{m-1}(n) \\ & + H_{eq}(n)^+.D_{m+1}(n) + W_m(n). \end{aligned} \quad (18)$$

The preceding interference model shows that subcarrier n encounters interference only from subcarrier n of the adjacent subbands. Hence, the interference across subbands can be handled by joint detection for each subcarrier over all subbands. That is, OFDM parallelizes the tasks of handling both inter-symbol interference and inter-band interference across subcarriers. We can now formulate the interference model for each specific subcarrier n across all subbands ($m = 1, \cdots, M$). Denoting the received signal for subcarrier n (after OFDM processing: removing the CP and taking DFT) across all subbands by $\mathbf{R}^{(n)}$, and the corresponding transmitted data over subcarrier n over all subbands by $\mathbf{d}^{(n)}$, the interference model for subcarrier n is as follows:

$$\mathbf{R}^{(n)} = \mathcal{H}^{(n)}\mathbf{D}^{(n)} + \mathbf{W}^{(n)}, \quad (19)$$

where

$$\mathbf{R}^{(n)} = [R_1(n), R_2(n), \cdots, R_M(n)]^T, \quad (20)$$

$$\mathbf{D}^{(n)} = [D_1(n), D_2(n), \cdots, D_M(n)]^T, \quad (21)$$

$$\mathbf{W}^{(n)} = [W_1(n), W_2(n), \cdots, W_M(n)]^T, \text{ and} \quad (22)$$

$$\mathcal{H}^{(n)} = \begin{bmatrix} H_{eq}(n) & H_{eq}^+(n) & 0 & \cdots & 0 \\ H_{eq}^-(n) & H_{eq}(n) & H_{eq}^+(n) & \cdots & 0 \\ 0 & H_{eq}^-(n) & H_{eq}(n) & \cdots & 0 \\ \vdots & & & & \\ 0 & 0 & 0 & \cdots & H_{eq}(n) \end{bmatrix}. \quad (23)$$

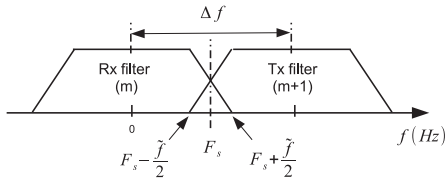

Fig. 7. Baseband equivalent model for subband m and the interfering subband $m+1$.

Data transmitted on subcarrier n can now be jointly detected across subbands using the model (19). For M parallel subbands and N subcarriers per subband, the maximum number of non-zero channel coefficients is $N \times (3M-2)$. Of course, we expect inter-band interference to be significant only at the edges of the subbands, hence the effort on interference suppression needs only be expended on edge subcarriers, as discussed in more detail in the next section.

B. Variation Across Subcarriers

Now that we have a per-subcarrier interference model, we ask how the interference structure varies across subcarriers. The analog transmit filter for subband $m \pm 1$ and the receive filter for subband m overlap only in their transition bands. Therefore, we expect that the subcarriers at the edges encounter more interference than those in the middle of the subband. In order to develop more specific insight, consider the baseband equivalent model for the interference due to subband $m+1$ seen by subband m (the interference due to subband $m-1$ follows an entirely analogous pattern).

Following (17), the coefficients of the effective interfering channel discrete Fourier transform (DFT) with size N, i.e. $\mathbf{H}_{eq}^{\pm}$, determines the amount of interference for each subcarrier. The effective interfering channel impulse response is defined in (13). The frequency response of the effective interfering channel is the product of the frequency responses of the receive filter (subband m), transmission channel h, and the transmit filter (subband $m+1$). Fig. 7 shows the frequency response of the receive filter for subband m and the transmit filter for subband $m+1$. The continuous time Fourier transform (CTFT) of the effective interfering subband (Hc^+) is approximately zero except for the overlapping region

$$\begin{cases} Hc^+(f) \approx 0 & \text{for } f < F_s - \tilde{f}/2 \\ Hc^+(f) \neq 0 & \text{for } F_s - \tilde{f}/2 < f < F_s + \tilde{f}/2 \end{cases}, \quad (24)$$

where $\tilde{f}$ denotes the amount of frequency overlap between subbands m and $m+1$, and F_s is the separation between the subband center frequencies. (In our system, the OFDM sampling rate $1/T = F_s$.) The frequency response of the sampled effective channel ($Hs^{(m+)}$) is related to the continuous time Fourier transform (CTFT) of the channel through aliasing:

$$Hs^+(f) = F_s \sum_{l=-\infty}^{+\infty} Hc^+(f - lF_s). \quad (25)$$

The discrete Fourier transform (DFT) with length N is derived by taking samples from one period of the sampled CFTF (25) at the sampling rate of N/F_s

$$H_{eq}^{+}(n) = Hs^{+}(nF_s/N) = \sum_{k=-\infty}^{+\infty} Hc^{+}\left(\frac{nF_s}{N} - kF_s\right) \quad \text{for } n = 0, \cdots, N-1. \tag{26}$$

Using (24) and (26), the DFT coefficients of interfering channel are

$$\begin{cases} H_{eq}^{+}(n) \neq 0 & \text{for } 0 \leq n < \dfrac{\tilde{f}N}{2F_s} \\ H_{eq}^{+}(n) \neq 0 & \text{for } N - \dfrac{\tilde{f}N}{2F_s} \leq n < N \\ H_{eq}^{+}(n) \approx 0 & \text{elsewhere.} \end{cases} \tag{27}$$

We observe that, due to aliasing, the effective interference from subband $m+1$ hits the OFDM subcarriers in subband m on both the left and right boundaries. Analogously, the interference from subband $m-1$ also hits the OFDM subcarriers on both boundaries. However, the middle subcarriers do not see interference (under reasonable assumptions on filter transition bands), hence the channel matrix (23) is diagonal for them. Thus, the receiver needs to perform joint data detection, or interference suppression, only for boundary subcarriers.

C. Interference Suppression

We investigate two linear channel equalization scenarios for joint detection of the boundary subcarriers. In the first scenario, we assume that the channel is perfectly known and we use a zero-forcing linear channel equalizer. In the second scenario, we consider a MMSE linear equalizer implemented using least squares adaptation based on a training sequence.

a) Zero-Forcing Linear Equalizer: Assuming that the channel matrix for each subcarrier ($\mathcal{H}_n$) is known at the receiver, a zero-forcing (ZF) linear equalizer for each OFDM subcarrier can be applied for joint detection of the transmitting symbols over the subbands. For the interference model (19), the ZF linear equalizer jointly estimates the symbols of subcarrier n through

$$\hat{\mathbf{D}}^{(n)} = \text{inv}(\mathcal{H}^{(n)})\mathbf{R}^{(n)}. \tag{28}$$

The ZF equalizer incurs noise enhancement, but based on the per-subcarrier interference model (19) and (23), we expect this to be significant only for the boundary subcarriers.

b) MMSE Linear Equalizer: The MMSE equalizer is amenable to training based adaptation. The estimated symbols are related to the received symbols for each subcarrier through

$$\hat{\mathbf{D}}^{(n)} = \mathbf{C}_n^H \mathbf{R}^{(n)}, \tag{29}$$

where ^{H} denotes matrix Hermitian operation, and $\mathbf{C}_n$ is the equalizer matrix for subcarrier n, chosen to minimize the mean squared error (MSE) given by

$$\min_C \mathbf{E}\{(\mathbf{D}^{(n)} - \hat{\mathbf{D}}^{(n)})^2\}, \tag{30}$$

where $\mathbf{E}\{.\}$ denotes the expectation operation. Substituting (29) into (30) and minimizing the mean square error by taking the derivative with respect to matrix $\mathbf{C}$, we get the standard solution:

$$\mathbf{C}_n = \text{inv}(\mathcal{R})\mathcal{P}, \tag{31}$$

where $\mathcal{R} = \mathbf{E}\{\mathbf{R}^{(n)}\mathbf{R}^{(n)^H}\}$ is the correlation matrix of the observations and the cross correlation matrix

$$\mathcal{P} = [\mathbf{E}\{(D_1(1))^H\mathbf{R}^{(n)}\} \cdots \mathbf{E}\{(D_2(n))^H\mathbf{R}^{(n)}\} \cdots \mathbf{E}\{(D_M(n))^H\mathbf{R}^{(n)}\}]. \tag{32}$$

As usual, for a least squares implementation, the preceding expectations are replaced by empirical averages, with the estimation of $\mathcal{P}$ requiring a training sequence.

V. Mismatch Analysis

We now analyze the effect of imperfect sampling-based channelization as in Fig. 5. The channelized employs polyphase sampling, just as in a time-interleaved ADC, hence can model the sampling impairments in analogous fashion. Typical impairment models include gain mismatch, timing mismatch and offset mismatch. While gain and offset mismatch can be handled more easily using calibration techniques, calibration of the timing mismatch (or static phase noise) is more challenging. We therefore focus on timing mismatch to illustrate the key concepts. We note that the effect of timing mismatch on the HRM mixer bank is studied in [39], and a calibration technique through AGC blocks has been proposed. In our setting, it is far easier to fold mismatch compensation into the interference suppression framework developed in the previous section.

For the system block diagram in Fig. 5, the transmitted signal is given by

$$y(lT + iT/M) = \sum_{n=-\infty}^{\infty}\left(\sum_{m=0}^{M-1} d_m(nT)e^{j2\pi mi/M}\right)P_T[(l-n)T + iT/M] = \sum_{n=-\infty}^{\infty} D_i(nT)P_T[(l-n)T + iT/M]. \tag{33}$$

where $D_i(nT)$ is the ith element of the $d_m(nT)$ Fourier transform. Assuming an ideal channel (for simplicity of exposition), the received signal, accounting for timing mismatch at the sampler, is given by

$$\hat{d}_k(nT) = \sum_{p=0}^{M-1}\sum_{l=-\infty}^{\infty} y(lT + pT/M + \delta_p) \times P_R\left[(n-l)T - pT/M\right]e^{-j2\pi pk/M} \tag{34}$$

where δ_p denotes the timing error (mismatch) for subband p. Considering the transmitted signal model, the received signal with unknown timing mismatch is

$$y(lT + pT/M + \delta_p) = \sum_{n=-\infty}^{\infty} D_p(nT)P_T[(l-n)T + pT/M + \delta_p], \tag{35}$$

where we have used $D_i(nT+\delta_p) = D_i(nT)$ since the amount of sampling time error is smaller than the symbol time duration. Substituting (35) in (34) and simplifying the results, we obtain

$$\hat{d}_k(mT) = \sum_{p=0}^{M-1}\left(\sum_{l=-\infty}^{\infty}\left(\sum_{n=-\infty}^{\infty}\sum_{q=0}^{M-1} d_q(nT)e^{j2\pi qp/M} P_T[(l-n)T+pT/M+\delta_p]\right) P_R\left[(m-l)T-kT/M\right]\right) e^{-j2\pi pk/M}. \quad (36)$$

By separating the above summation into the desired received signal ($n=m$ and $p=k$), the inter symbol interference term ($n\neq m$ and $p=k$), and the inter-band interference term ($p\neq k$), we have

$$\begin{aligned}\hat{d}_k(mT) =& d_k(mT)h_{k,k}(mT,mT) \\ &+ \sum_{\substack{n=-\infty \\ n\neq m}}^{\infty} d_k(nT)h_{k,k}(nT,mT) \\ &+ \sum_{\substack{p=0 \\ p\neq k}}^{M-1} d_p(nT)h_{p,k}(mT,mT) \\ &+ \sum_{\substack{p=0 \\ p\neq k}}^{M-1}\sum_{\substack{n=-\infty \\ n\neq m}}^{+\infty} d_p(nT)h_{p,k}(nT,mT) \end{aligned} \quad (37)$$

where

$$\begin{aligned}h_{p,k}(mT,nT) =& \\ &\sum_{l=-\infty}^{\infty} e^{j2\pi(f_p-f_k)kT_c} P_T(lT-mT+pT/M+\delta_p) \\ &\times P_R(nT-lT-kT/M), \end{aligned} \quad (38)$$

is the equivalent channel from transmit subband p at time mT to the receive subband k at time nT. Note that the transmitted data samples $d_p(mT)$ are OFDM samples transmitted on subband p. Therefore, additional ISI due to timing mismatch, second term in (37), is also handled by frequency domain equalization in OFDM processing.

In case of timing mismatch, the inter-band interference term that appears in the third row of (37) follows the same per-subcarrier structure as in Section IV. However, we expect that more subcarriers experience inter-band interference since the filters are more overlapped. The last term in (37) is the inter-band interference from the symbols of other time samples which we assume that it is negligible since the timing mismatch, which is supposed to be a fraction of the signal symbol time (T/M), is small in comparison to the OFDM symbol time T on each symbol. Therefore, considering standard pulse shaping filters such as SRRC, that small variation is negligible and the orthogonality between the OFDM symbols transmitted at different times from different subbands is well preserved.

VI. Performance on Indoor mm-Wave Channels

We now provide insight into the performance of the proposed scheme via simulations based on an indoor mm-wave channel model.

A. mm-Wave Channel for Indoor Applications

We have considered the IEEE 802.11ad standard mm-wave channel model [1] which is based on ray-tracing simulations and experimental measurements. This standard model draws on the quasi-optical nature of the mm-wave signal to model the channel based on a small number of paths including line of sight path (LoS), first-order reflection paths, and second order reflection paths. Each path in this standard is modeled as a cluster of closely spaced rays [40]. Therefore, within each path, we expect to see a frequency selective channel over a large bandwidth (e.g. 66 MHz bandwidth [41]). The statistical models for the paths and the intra-cluster parameters are provided by the standard [1], [41] and are used in our simulations.

Mm-wave signal transmission systems suffer from large propagation loss due to the small wavelength (Friis' equation). In the link budget, the large propagation loss is compensated with the directivity gain of the antenna arrays that is achievable in a compact form factor due to the small wavelength. Additionally, directional transmission between the transmitter and the receiver over one selected strong path reduces the delay-spread of the mm-wave channel. In this work, we assume that the transmitter and receiver are each equipped with 4×4 square arrays with $\lambda/2$ element spacing, and that these are both steered towards the strongest path.

We observed through the simulations that the delay spread of the mm-wave channel impulse response even after the beamforming is still large. As an example, in one realization of the beamformed conference room channel, the delay spread as large as 12 ns is observed [20]. The possibly large delay spread after the beamforming is due to the leakage from other eliminated strong paths which are in close angular proximity with the main select beamformed path. The other source of the delay spread is due to cluster-based ray-tracing model where closely spaced rays existed within the beamformed path. However, the delay spread due to intra-cluster rays is limited to a few ns [41] which can be neglected in comparison to the multi-path delay spread. Large delay spread realizations observed after beamforming validates the design concept of using OFDM with CP over the subbands to simplify the equalization model at the receiver side for handling ISI.

B. Simulation Parameters

We set the OFDM subband symbol rate of $1/T = F_s = 250$ MHz throughout the simulations. The carrier frequency is 60 GHz. We assume $N = 64$ subcarriers for OFDM over each subband, with a cyclic prefix of 16 samples. We assume 16QAM modulation. With these parameters, if we use 16 subbands, we can attain a rate of 12.8 Gbps using off-the-shelf ADCs, ignoring channel coding overhead. (We do not model

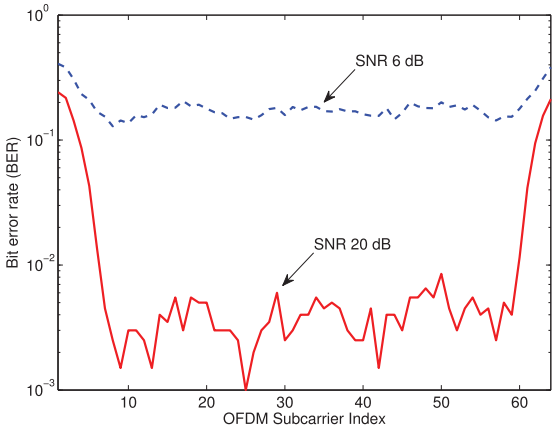

Fig. 8. BER vs. OFDM subcarrier for one realization of the channel when inter-band interference is not suppressed. BER decays with increasing SNR except for boundary subcarriers, which encounter interference from adjacent subbands.

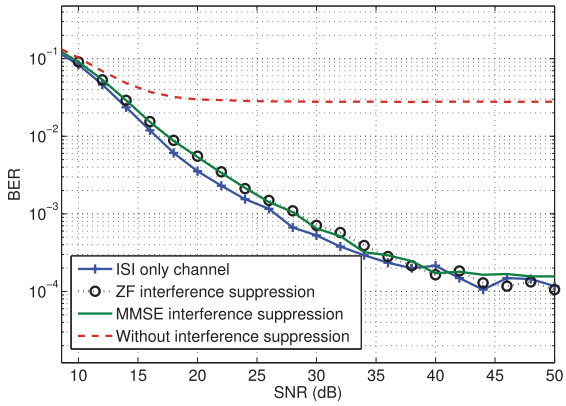

Fig. 9. BER v.s. SNR without inter-band interference suppression, with zero-forcing and MMSE linear equalizers, and the benchmark ISI only channel. The BER is averaged over 1000 independent channel scenarios and transmit data streams.

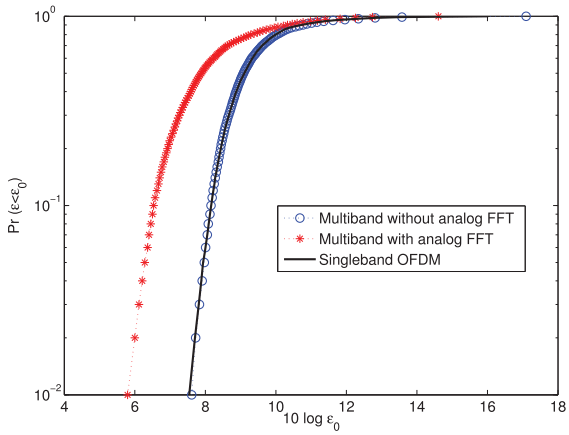

Fig. 10. Empirical distribution of the PAR for a multiband scenario with $M = 16$ OFDM subbands, each contains $N = 64$ subcarriers.

channel coding here, since we are focusing on inter-band interference, but we expect the coding to be fairly lightweight, with small overhead, in high SNR indoor settings.)

Since interference is encountered only from adjacent subbands, we only consider a simulation scenario with three consecutive subbands ($M = 3$) and focus on the performance of the middle subband, averaging over channel realizations. The latter are generated using the conference room scenario as described in IEEE 802.11-09 for 60 GHz carrier frequency [1]. In order to model the effect of channel dispersion, we assume throughout that the line of sight path is blocked, and the transmitter and receiver steer their arrays towards the strongest non-LoS path. We modeled the transmit and the receive filters, used in evaluating the baseband equivalent channels (12), (14), and (13), by the squared root raised cosine (SRRC) filter with excess bandwidth of 1.125.

C. Performance Analysis

For performance evaluation, we average the bit error rate (BER) over 1000 independent realizations of the indoor conference room channel and the transmitted signal. Since ISI is handled with CP insertion, the ISI-only channel with no inter-band interference is the performance benchmark against which we compare our interference suppression schemes. As mentioned, we report only on the performance of the middle of three subbands.

Fig. 8 shows the BER as a function of subcarrier index without interference suppression, for SNR of 6 and 20 dB. We note that, as SNR increases, BER decays except for the boundary subcarriers, confirming that a performance floor due to interference from adjacent subbands appears only for the boundary subcarriers.

Fig. 9 compares BER performance of a system with no interference suppression, the ZF and MMSE interference suppression, and the benchmark ISI-only channel. Clearly, OFDM with the given cyclic prefix is effective in dealing with the ISI of the beamformed channel, but inter-band interference can significantly degrade performance (error floor of 3×10^{-2} after 20 dB SNR) unless suppressed. Both ZF and MMSE equalizers yield performance close to the ISI-only benchmark. For the ZF equalizer, we assumed that the channel state information for each subcarrier is known at the receiver. However, the MMSE linear equalizer is trained based on 50 OFDM training symbols. For the quasi-static indoor channels of interest, we expect that such training would be needed quite seldom (e.g., when starting up a link), with continuing adaptation in decision-directed mode.

D. Peak to Average Power Ratio

In Section III, we note that the PAR reduces after performing sampled analog FFT, relative to that of OFDM over the entire band digitized using a time-interleaved ADC. In this section, we numerically evaluate the PAR of the simulated AMT system. We consider both an ideal and a simulated mm-wave channel.

Fig. 10 shows the empirical distribution of the PAR for AMT system structure presented in Fig. 5. We have considered $M = 16$ subbands for this simulation and each subband carries OFDM samples with $N = 64$ subcarriers. The PAR for three different scenarios that covers the total bandwidth are compared with each other. In the first scenario, the low rate ADCs are

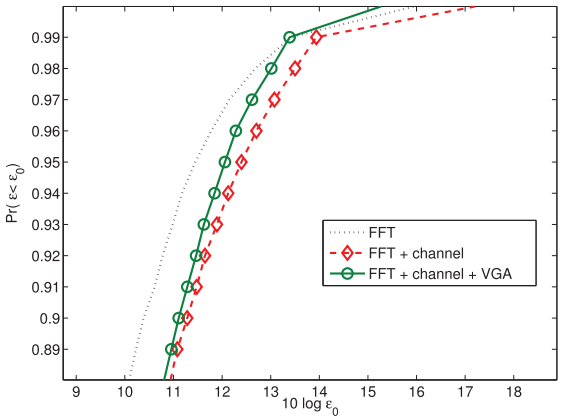

Fig. 11. Empirical distribution of the PAR for a multiband scenario considering the effect of mm-wave channel.

located after the S/P block and the DFT is handled in digital domain. This may be interpreted as digital filtered multitone, similar to Fig. 5 except that the ADCs are located after the S/P conversion. The second scenario is our proposed analog-DFT based channelizer in Fig. 5, with PAR calculated after the analog DFT block. The third corresponds to OFDM over the entire band, with $M \times N$ subcarriers; the sub-ADCs for a TI-ADC digitizing such a system would see this PAR.

We observe from Fig. 10 that the analog DFT significantly reduces the maximum PAR seen by low-rate ADCs. Of course, the dynamic range is expected to increase when we account for channel dispersion. In order to study this, we consider the effective channel corresponding to the 802.11ad standard indoor conference room model after beamforming along the dominant path, and evaluate the empirical distribution of the PAR over 5000 independent realizations of the channel and transmitted data. The results are plotted in Fig. 11. Comparing with Fig. 10, we note that our proposed approach still leads to PAR reduction, but the advantage is reduced, especially in the high percentile regions of the plot, because of channel frequency selectivity. However, we can mitigate the effect of frequency selectivity across subbands by applying a separate variable gain amplifier (VGA) for each subband after the analog DFT, and prior to ADC. The VGAs normalize the short-term average of the received power on each subband to a nominal value, and, as shown in Fig. 11, reduce the PAR in the high percentile regions of the plot.

E. Mismatch Analysis

We now study the performance of the proposed system in the presence of timing mismatch at the polyphase sampler. We observed in Section V that timing mismatch increases both intersymbol and inter-band interference. However, the OFDM CP easily handles the excess dispersion due to mismatch, hence the inter-band interference is the key impact to be studied. In essence, timing mismatch spreads out the effective interfering channels seen by adjacent subbands. To see this, we plot in Fig. 12 the BER as a function of OFDM subcarrier index in the presence of mismatch, when interference suppression is not applied. We see that a larger number of edge subcarriers suffer

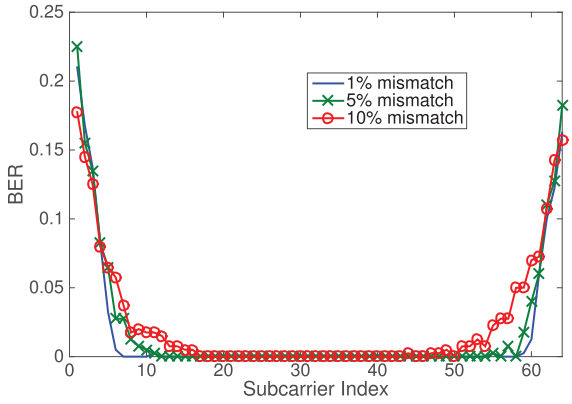

Fig. 12. BER per OFDM subcarrier of the transmit channel when 10% timing mismatch happens at the sampler.

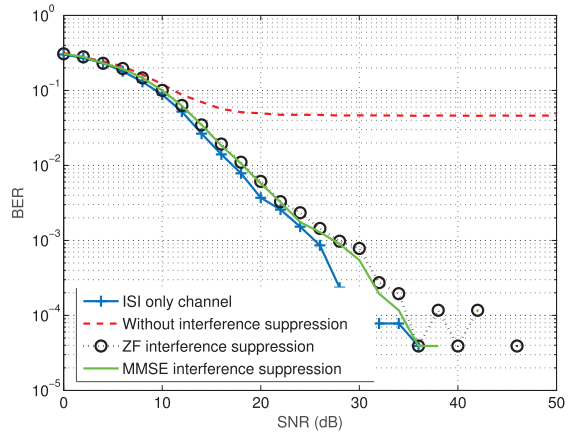

Fig. 13. Overall performance of the analog multiband system with 10% timing mismatch at the receiver sampler. Comparing with Fig. 9, we observe that the MMSE and ZF equalizers handle the timing mismatch effectively.

from an interference floor, compared to the no-mismatch setting of Fig. 8. Thus, our per-subcarrier interference suppression scheme must be applied to more subcarriers.

Fig. 13 shows the BER (averaged over subcarriers) in the presence of timing mismatch for MMSE and zero-forcing per-subcarrier interference suppression. In comparison with Fig. 9 (no mismatch), the error floor when no interference suppression scheme is applied is higher in the presence of timing mismatch, but linear interference suppression is still successful in removing error floors, since the equalizer is trained on the effective channel seen at the receiver, and automatically incorporates the effect of timing mismatch.

F. Effect of Pulse Shaping Filter Selection

We now investigate the effect of pulse shaping filters on the proposed system in Fig. 5. In direct channelization using a bank of HRM mixers, the lowpass filters are applied for rejecting residual harmonics. These filters are generally more relaxed than the polyphase filters required for channelization based on the sampled analog FFT. This is because in a HRM mixer tuned on frequency nf_{LO}, all harmonic frequencies are rejected except for $Lf_{LO} - nf_{LO}$. In contrast, in the proposed sampled

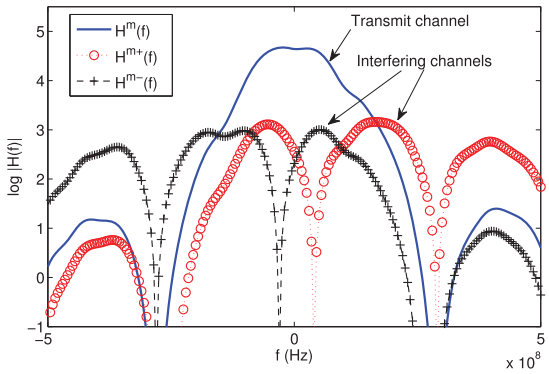

Fig. 14. Frequency responses of the equivalent desired channel and the adjacent interfering channels for filtering with rectangular time domain impulse response.

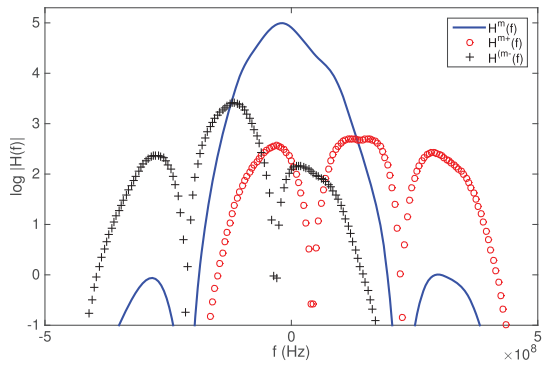

Fig. 15. Frequency responses of the equivalent desired channel and the adjacent interfering channels for IOTA filtering.

analog FFT based channelizer, the polyphase filters play a crucial role in shaping the subbands. In order to investigate the importance of the choice of the underlying pulse shaping filter on system performance, we consider three options: SRRC filter with roll off factor of 1.125 (used in all of our numerical results thus far), rectangular time domain pulse (which has large sidelobes in the frequency domain), and the isotropic orthogonal transform algorithm (IOTA) pulse shaping filters, which provides a balance between filter length and spectral containment.

Figures 14, 15, and 16 show the frequency response of the equivalent transmit and interfering channels (for an indoor mm-wave channel) for the different choices of pulse shaping. For the rectangular time domain pulse, we observe from Fig. 14 that the leakage from the interfering channels is spread over the entire transmit band. For the IOTA filters, we observe that the leakage is still significant, but decays much faster than for the rectangular pulse, with the inter-band interference still limited to a number of edge subcarriers. For SRRC with roll-off factor $\alpha = 0.125$ (Fig. 16), the inter-band interference is limited to a small number of subcarriers at the boundaries of the transmit band.

Fig. 17 compares the BER per OFDM subcarrier of the transmit channel for the different filter choices. The SNR is fixed to a high value of 40 dB, and interference suppression is not applied, hence the BER is dominated by interference. We see that the rectangular pulse incurs an interference floor across all subcarriers, while only the edge subcarriers are affected for the

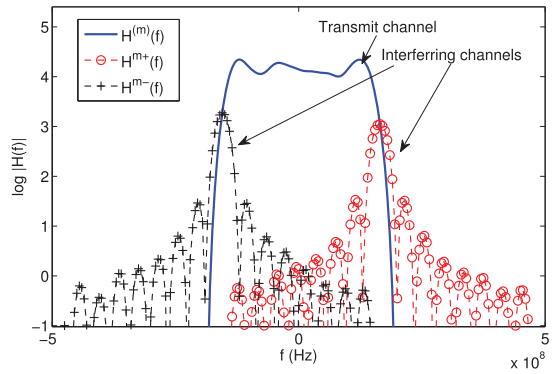

Fig. 16. Frequency responses of the equivalent desired channel and the adjacent interfering channels for SRRC filtering.

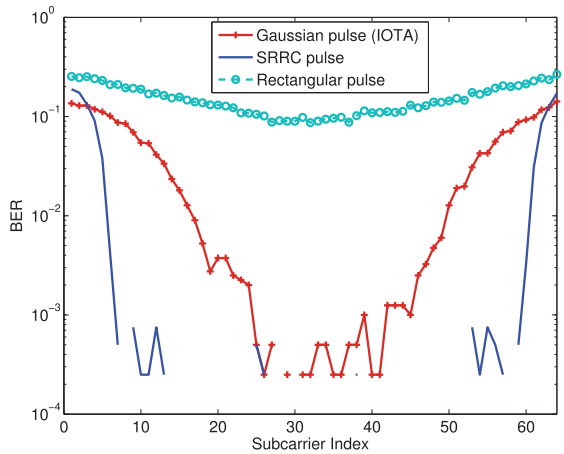

Fig. 17. BER per OFDM subcarrier when rectangular filters, IOTA filters, or SRRC filters are applied.

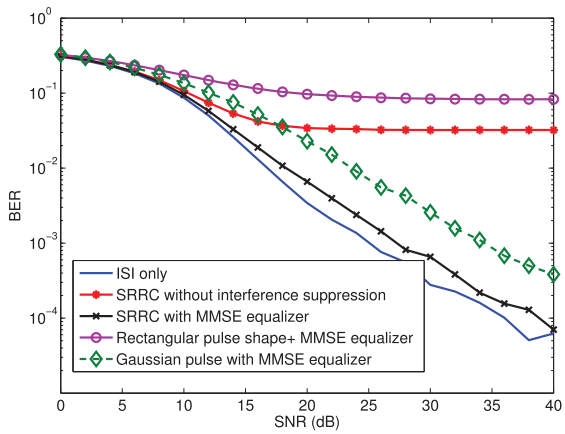

Fig. 18. BER vs. SNR for rectangular, IOTA and SRRC filters. For rectangular filters, the inter-band interference spreads over all subcarriers, and linear interference suppression based on the adjacent bands does not work. For IOTA and SRRC filters, the interference is spectrally contained, and our interference suppression scheme is effective.

IOTA and SRRC filters (the error floors span more subcarriers for IOTA than for SRRC).

Fig. 18 compares the overall BER performance across filter choices when interference suppression is applied. We see that interference suppression is ineffective for the rectangular pulse. The SRRC filter attains performance close to the ISI-only

benchmark, while the IOTA filter attains slightly worse performance, but without an error floor (thus, the latter incurs larger noise enhancement but linear interference suppression still works).

VII. Conclusions

Analog channelization into subbands has several important advantages for scaling up communication bandwidths: (a) for a given channel delay spread, the effective channel length in terms of number of symbols is smaller, reducing the complexity and overhead of equalization; (b) the digitization required for applying sophisticated DSP algorithms is parallelized, so that slower ADCs can be employed; (c) the dynamic range of the input to the ADCs is reduced, since it corresponds to signal variations across a subband rather than over the entire band. While a direct approach to channelization using a mixer bank suffers from hardware complexity and coupling, the sampled analog FFT with polyphase filters is a promising approach. For OFDM within each subband, a per-subcarrier interference linear suppression framework is effective, provided that the filters used for channelization are well designed. This framework is also able to handle the additional interference produced by timing mismatch. Thus, analog multiband with OFDM provides an attractive approach for scaling modern DSP-centric communication techniques to large bandwidths while handling significant channel dispersion, by coupling sloppy analog channelization with DSP-centric techniques for combating inter-band interference, intersymbol interference and imperfections in channelization. For the nominal designs driving our simulation models, off-the-shelf ADCs running at 250 MHz can be used to attain data rates of 12.8 Gbps over 4 GHz of bandwidth.

It is possible to attain even larger data rates than the preceding estimates by layering on spatial multiplexing, which is feasible with compact node form factors even in LoS environments [42], hence an important topic for future work is design and performance evaluation of combining bandwidth scaling with spatial multiplexing. Also, while we consider OFDM within each subband because of its technological maturity, single carrier techniques deserve deeper exploration because of their smaller dynamic range.

Our goal in this paper is to present the proposed architecture as an interesting alternative to a standard all-digital design with TI-ADC based digitization, as a means of continuing to push the limits of communication bandwidth. Of course, determining the winning design in any given context requires much further work involving detailed circuit-level tradeoffs of power, cost and performance. For the proposed architecture, passive channelization techniques [26], [27] present an intriguing possibility requiring further study as to whether they can scale in bandwidth, and how nonlinearities impact inter-band interference.

Acknowledgment

The authors acknowledge the help and feedback from researchers in Samsung Research America - Dallas on this work.

References

[1] *Channel Models for 60 GHz WLAN Systems*, IEEE 802.11-09/0334r8, 2010.
[2] S. Rajagopal, S. Abu-Surra, Z. Pi, and F. Khan, "Antenna array design for multi-Gbps mmwave mobile broadband communication," in *Proc. IEEE Global Telecommun. Conf. (GLOBECOM'11)*, Dec. 2011, pp. 1–6.
[3] T. Kim, J. Park, J. Y. Seol, S. Jeong, J. Cho, and W. Roh, "Tens of Gbps support with mmwave beamforming systems for next generation communications," in *Proc. IEEE Global Commun. Conf. (GLOBECOM)*, Dec. 2013, pp. 3685–3690.
[4] T. Rappaport *et al.*, "Millimeter wave mobile communications for 5G cellular: It will work!" *IEEE Access*, vol. 1, pp. 335–349, May 2013.
[5] Y. Zhu *et al.*, "Demystifying 60 GHz outdoor picocells," in *Proc. 20th Annu. Int. Conf. Mobile Comput. Netw.*, 2014, pp. 5–16.
[6] B. Murmann. *ADC Performance Survey 1997–2015*, 2015 [Online]. Available: http://web.stanford.edu/∼murmann/adcsurvey.html
[7] A. Amirkhany, V. Stojanovic, and M. Horowitz, "Multi-tone signaling for high-speed backplane electrical links," in *Proc. IEEE Globecom*, Mar. 2004, vol. 2, pp. 1111–1117.
[8] A. Amirkhany *et al.*, "A 24 Gb/s software programmable analog multi-tone transmitter," *IEEE J. Solid-State Circuits*, vol. 43, no. 4, pp. 999–1009, Feb. 2008.
[9] A. Klekamp, R. Dischler, and F. Buchali, "Limits of spectral efficiency and transmission reach of optical-OFDM superchannels for adaptive networks," *IEEE Photon. Technol. Lett.*, vol. 23, no. 20, pp. 1526–1528, Oct. 2011.
[10] M. Rodwell *et al.*, "Optical phase-locking and wavelength synthesis," in *Proc. IEEE Compound Semicond. Integr. Circuit Symp. (CSICs)*, Oct. 2014, pp. 1–4.
[11] V. Dyadyuk *et al.*, "A multigigabit millimeter-wave communication system with improved spectral efficiency," *IEEE Tran. Microw. Theory Techn.*, vol. 55, no. 12, pp. 2813–2821, Dec. 2007.
[12] H. Zhang, S. Venkateswaran, and U. Madhow, "Analog multitone with interference suppression: Relieving the ADC bottleneck for wideband 60 GHz systems," in *Proc. IEEE GLOBECOM*, Mar. 2012, pp. 2305–2310.
[13] M. Lehne and S. Raman, "A discrete-time FFT processor for ultrawideband OFDM wireless transceivers: Architecture and behavioral modeling," *IEEE Trans. Circuits Syst.*, vol. 57, no. 11, pp. 3011–3022, Nov. 2010.
[14] G. Wunder *et al.*, "5GNOW: Non-orthogonal, asynchronous waveforms for future mobile applications," *IEEE Commun. Mag.*, vol. 52, no. 2, pp. 97–105, Feb. 2014.
[15] M. Mishali and Y. Eldar, "From theory to practice: Sub-Nyquist sampling of sparse wideband analog signals," *IEEE J. Sel. Topics Signal Process.*, vol. 4, no. 2, pp. 375–391, Apr. 2010.
[16] J. I. Tamir, T. S. Rappaport, Y. C. Eldar, and A. Aziz, "Analog compressed sensing for RF propagation channel sounding," in *Proc. IEEE Int. Conf. Acoust. Speech Signal Process. (ICASSP)*, Mar. 2012, pp. 5317–5320.
[17] D. Ramasamy, S. Venkateswaran, and U. Madhow, "Compressive adaptation of large steerable arrays," in *Proc. Inf. Theory Appl. Workshop (ITA)*, Feb. 2012, pp. 234–239.
[18] F. Schaich and T. Wild, "Waveform contenders for 5G; OFDM vs. FBMC vs. UFMC," in *Proc. 6th Int. Symp. Commun. Control Signal Process. (ISCCSP)*, May 2014, pp. 457–460.
[19] G. Fettweis, M. Krondorf, and S. Bittner, "GFDM—Generalized frequency division multiplexing," in *Proc. IEEE 69th Veh. Technol. Conf. (VTC-Spring)*, Apr. 2009, pp. 1–4.
[20] H. Roufarshbaf, U. Madhow, and S. Rajagopal, "OFDM-based analog multiband: A scalable design for indoor mm-wave wireless communication," in *Proc. IEEE GLOBECOM*, Dec. 2014, pp. 3267–3272.
[21] H. Roufarshbaf, U. Madhow, M. Rodwell, and S. Rajagopal, "Efficient analog multiband channelization for bandwidth scaling in mm-wave systems," in *Proc. IEEE Int. Conf. Commun. (ICC)*, Jun. 2015, pp. 1316–1321.
[22] B. Farhang-Boroujeny, "OFDM versus filter bank multicarrier," *IEEE Signal Process. Mag.*, vol. 28, no. 3, pp. 92–112, May 2011.
[23] T. Forbes, W. G. Ho, and R. Gharpurey, "Design and analysis of harmonic rejection mixers with programmable LO frequency," *IEEE J. Solid-State Circuits*, vol. 48, no. 10, pp. 2363–2374, Oct. 2013.
[24] C. Andrews and A. C. Molnar, "A passive mixer-first receiver with digitally controlled and widely tunable RF interface," *IEEE J. Solid State Circuits*, vol. 45, no. 12, pp. 2696–2708, Dec. 2010.
[25] J. Weldon *et al.*, "A 1.75-GHz highly integrated narrow-band CMOS transmitter with harmonic-rejection mixers," *IEEE J. Solid State Circuits*, vol. 36, no. 12, pp. 2003–2015, Dec. 2001.

[26] Y. C. Ou and G. M. Rabeiz, "A 20-90 MHz 26-channel cochlear-based channelizer," in *Proc. IEEE Int. Microw. Symp.*, May 2010, pp. 213–216.
[27] J. P. Magalhaes, T. Monteiro, R. Gomez-Garcia, and N. B. Carvalho, "Papoulis-Gerchberg hybrid filter bank receiver for cognitive-/software defined radio systems," in *Proc. IEEE Int. Symp. Circuits Syst.*, May 2013, pp. 69–72.
[28] G. Cherubini, E. Eleftheriou, and S. Olcer, "Filtered multitone modulation for very high-speed digital subscriber lines," *IEEE Trans. Sel. Area Commun.*, vol. 20, no. 5, pp. 1016–1028, Jun. 2002.
[29] A. D. S. Jayalath and C. R. N. Athaudage, "On the PAR reduction of OFDM signals using multiple signal representation," in *Proc. IEEE Int. Symp. Pers. Indoor Mobile Radio Commun.*, Sep. 2003, pp. 799–803.
[30] A. Tolmachev and M. Nazarathy, "Real-time-realizable Filtered-Multi-Tone (FMT) Modulation for Layered-FFT Nyquist WDM Spectral Shaping," in *37th Eur. Conf. Expo. Opt. Commun.*, Optical Society of America, 2011, pp. We.10.P1.65 [Online]. Available: http://www.osapublishing.org/abstract.cfm?URI=ECOC-2011-We.10.P1.65.
[31] F. Houfaf, M. Egot, A. Kaiser, A. Cathelin, and B. Nauta, "A 65 nm CMOS 1-to-10 GHz tunable continuous-time low-pass filter for high-data-rate communications," in *Proc. IEEE Int. Solid-State Circuits Conf. (ISSCC) Dig. Tech. Papers*, Feb. 2012, pp. 362–364.
[32] M. Seo, M. J. Rodwell, and U. Madhow, "Comprehensive digital correction of mismatch errors for a 400-msamples/s 80-dB SFDR time-interleaved analog-to-digital converter," *IEEE Trans. Microw. Theory Techn.*, vol. 53, no. 3, pp. 1072–1082, Mar. 2005.
[33] P. Sandeep, U. Madhow, M. Seo, and M. Rodwell, "Joint channel and mismatch correction for OFDM reception with time-interleaved ADCs: Towards mostly digital multiGigabit transceiver architectures," in *Proc. IEEE GLOBECOM*, Nov. 2008, pp. 1–5.
[34] E. Z. Tabasy, A. Shafik, K. Lee, S. Hoyos, and S. Palermo, "A 6 bit 10 GS/s TI-SAR ADC with low-overhead embedded FFE/DFE equalization for wireline receiver applications," *IEEE J. Solid-State Circuits*, vol. 49, no. 11, pp. 2560–2574, Nov. 2014.
[35] S. L. Tual, P. N. Singh, C. Curis, and P. Dautriche, "22.3 a 20 GHz-BW 6b 10 GS/s 32 mW time-interleaved SAR ADC with master T&H in 28 nm UTBB FDSOI technology," in *Proc. IEEE Int. Conf. Solid-State Circuits*, Feb. 2014, pp. 382–383.
[36] S. Daneshgar, Z. Griffith, M. Seo, and M. Rodwell, "Low distortion 50 GSamples/s track-hold and sample-hold amplifiers," *IEEE J. Solid-State Circuits*, vol. 49, no. 10, pp. 2114–2126, Oct. 2014.
[37] M. Shunli, Y. Hao, and R. Junyan, "A 32.5-GS/s sampler with time-interleaved track-and-hold amplifier in 65-nm CMOS," *IEEE Trans. Microw. Theory Techn.*, vol. 62, no. 12, pp. 3500–3511, Dec. 2014.
[38] H. Pekau and J. W. Haslett, "A 2.4 GHz CMOS subsampling mixer with integrated filtering," *IEEE J. Solid-State Circuits*, vol. 40, no. 11, pp. 2159–2166, Nov. 2005.
[39] T. Forbes and R. Gharpurey, "A 2 GS/s frequency-folded ADC-based broadband sampling receiver," *IEEE J. Solid-State Circuits*, vol. 49, no. 9, pp. 1971–1983, Sep. 2014.
[40] H. Xu, V. Kukshya, and T. S. Rappaport, "Spatial and temporal characteristics of 60 GHz indoor channels," *IEEE J. Sel. Areas Commun.*, vol. 20, no. 3, pp. 620–630, Apr. 2002.
[41] A. Maltsev, R. Maslennikov, A. Lomayev, A. Sevastyanov, and A. Khoryaev, "Statistical channel model for 60 GHz WLAN systems in conference room environment," *Radioengineering*, vol. 20, no. 2, pp. 409–422, Jun. 2011.
[42] E. Torkildson, U. Madhow, and M. Rodwell, "Indoor millimeter wave MIMO: Feasibility and performance," *IEEE Trans. Commun.*, vol. 10, no. 12, pp. 4150–4160, Dec. 2011.

Hossein Roufarshbaf (S'07–M'11) received the Ph.D. degree in electrical engineering from George Mason University, Fairfax, VA, USA, in 2011. He is a Senior Staff System Design Engineer with Broadcom Limited. He has worked as a Postdoctoral Research Associate in a NASA founded research with University of Maine, ME, USA, as a Research Assistant Professor with George Mason University, VA, USA, and as a Postdoctoral Research Associate with University of California, Santa Barbara, CA, USA. His research interests include power-efficient system design for high-speed 5G wireless communication systems including mm-wave and WiFi access systems, statistical signal processing, navigation and tracking, machine learning, and statistical inference. He was the recipient of the Volgenau School of Engineering, Outstanding Graduate Student Award in 2011.

Upamanyu Madhow (S'86–M'90–SM'96–F'05) received the bachelor's degree in electrical engineering from the Indian Institute of Technology Kanpur, Kanpur, India, in 1985, and the Ph.D. degree in electrical engineering from the University of Illinois Urbana-Champaign, Champaign, IL, USA, in 1990. He is a Professor of Electrical and Computer Engineering with the University of California, Santa Barbara, Santa Barbara, CA, USA. He has worked as a Research Scientist with Bell Communications Research, Morristown, NJ, USA, and as a Faculty at the University of Illinois, Urbana-Champaign. His research interests include communications, signal processing and networking, with current emphasis on millimeter wave communication, and on distributed and bio-inspired approaches to networking and inference. He is the author of two textbooks *Fundamentals of Digital Communication* (Cambridge University Press, 2008) and *Introduction to Communication Systems* (Cambridge University Press, 2014). He has served as an Associate Editor for the IEEE TRANSACTIONS ON COMMUNICATIONS, the IEEE TRANSACTIONS ON INFORMATION THEORY, and the IEEE TRANSACTIONS ON INFORMATION FORENSICS AND SECURITY. He was the recipient of the 1996 NSF CAREER Award, and corecipient of the 2012 IEEE Marconi Prize Paper Award in wireless communications.

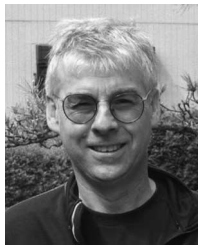

Mark Rodwell (F'03) received the Ph.D. degree from Stanford University, Stanford, CA, USA, in 1988. He holds the Doluca Family Endowed Chair of Electrical and Computer Engineering with University of California, Santa Barbara (UCSB), Santa Barbara, CA, USA. He also manages the UCSB Nanofabrication Laboratory. His research group develops nm and THz transistors, and millimeter-wave and THz integrated circuits. The work of his group and collaborators has been recognized by the 2010 IEEE Sarnoff Award, the 2012 IEEE Marconi Prize Paper Award, the 1997 IEEE Microwave Prize, the 1998 European Microwave Conference Microwave Prize, and the 2009 IEEE IPRM Conference Award.

Sridhar Rajagopal (M'98–SM'09) received the M.S. and Ph.D. degrees in electrical and computer engineering from Rice University, Houston, TX, USA. He is a Senior Staff R&D Engineer with Samsung Research America in Dallas, TX, USA. He has previously worked with WiQuest Communications in Allen, a UWB start-up and with Nokia Research Center in Irving. He is currently investigating technologies for 5G communication systems. He is an Associate Editor for the *Journal of Signal Processing Systems*.